Tech Science Press

LES Investigation of Drag-Reducing Mechanism of Turbulent Channel Flow with Surfactant Additives

Jingfa Li[1], Bo Yu[1,*], Qianqian Shao[2] and Dongliang Sun[1]

[1]School of Mechanical Engineering, Beijing Key Laboratory of Pipeline Critical Technology and Equipment for Deepwater Oil & Gas Development, Beijing Institute of Petrochemical Technology, Beijing, 102617, China
[2]Guangdong University of Petrochemical Technology, Maoming, 525000, China
*Corresponding Author: Bo Yu. Email: yubobox@vip.163.com

Abstract: In this work, the drag-reducing mechanism of high-Reynolds-number turbulent channel flow with surfactant additives is investigated by using large eddy simulation (LES) method. An N-parallel finitely extensible nonlinear elastic model with Peterlin's approximation (FENE-P) is used to describe the rheological behaviors of non-Newtonian fluid with surfactant. To close the filtered LES equations, a hybrid subgrid scale (SGS) model coupling the spatial filter and temporal filter is applied to compute the subgrid stress and other subfilter terms. The finite difference method and projection algorithm are adopted to solve the LES governing equations. To validate the correctness of our LES method and in-house code, the particle image velocimetry (PIV) experiment is carried out and representative measured results are compared with LES results in detail. Then the flow characteristics and drag-reducing mechanism of turbulent channel flow with surfactant are investigated from the perspective of drag reduction rate, mean velocity, fluctuation of deformation rate, shear stress, transport and dissipation of turbulent kinetic energy, and turbulent coherent structures. This research can shed a light on the application of turbulent drag reduction technique in district heating, petroleum transport, etc.

Keywords: Large eddy simulation; turbulent flow; drag reduction; hybrid subgrid scale model; N-parallel FENE-P model; PIV experiment

1 Introduction

Turbulent flow is pervasive in nature and engineering systems, for example, motion of atmosphere, flow of river, district heating, petroleum transport, nuclear engineering, etc. [1,2]. With rapid development of relevant technologies, the research on turbulent flow is growing faster nowadays than ever before. A wide range of applications has been found in nearly all aspects of fluid dynamics associated with turbulent flow, which mainly focus on either the enhancement of turbulence or the suppression of turbulence. Especially, as a major approach to relieve influences of turbulence on fluid flow behaviors, the interesting phenomenon that adding a little amount of additives (such as polymer, surfactant) to the turbulent flow would induce an appreciable

reduction of friction drag, which is called the turbulent drag reduction (DR), has attracted increasing attention from the academic and engineering communities [3–6].

Although the turbulent DR technique has been widely applied in many engineering problems in past decades, considerable gaps still remain in the understanding of drag-reducing mechanism, which is still open for discussion [7,8]. To investigate the drag-reducing mechanism induced by various drag reducers (especially the surfactant) in more details, in addition to experimental and theoretical approaches, the numerical simulation has been one of the most significant tools for turbulent studies. Commonly used numerical methods include direct numerical simulation (DNS) [9], large eddy simulation (LES) [10], Reynolds average Navier–Stokes (RANS) simulation [11], and hybrid simulation method, such as the detached eddy simulation (DES) [12] in which the closure is a modification to the production/destruction term of the original RANS model, reducing to RANS in the attached region and to LES away from the wall. Among the aforementioned numerical methods, DNS is capable to display detailed three-dimensional (3D) results at any time and any space and provide much deeper insight into the physics of microstructure-turbulence interaction. However, DNS has high demand on the computational workload and resources. To alleviate the computational burden of DNS, LES and RANS have been developed as efficient numerical techniques for the solution of turbulent flows in the presence of limited computing resources and high-Reynolds number. Compared with RANS modeling, LES strikes a satisfactory balance between the computational workload and simulation accuracy from the perspective of mechanism studies of turbulent flow. Thus LES has gained extensive attention and becomes the research hot-spot in turbulent simulations [13].

No matter for Newtonian turbulent flow or turbulent drag-reducing flow, current efforts in LES studies are weighted toward the accurate subgrid scale (SGS) model. In the past 50 years, the numerical modeling of SGS model for Newtonian turbulent flow has long been a subject of interest, and there exists a large body of literature addressing this topic [14–17]. Up to present, applications of LES in the numerical study of Newtonian turbulent flow are relatively mature. However, the development of SGS model in the presence of non-Newtonian turbulent flow is still in its infancy and more efforts are needed. Two notable problems associated with the SGS model for non-Newtonian turbulent flow are that the prediction accuracy of SGS model is still unsatisfactory and the SGS model for constitutive equations is still lacking. Another difficulty arises from the fact that the accurate modeling of rheological behaviors (such as apparent viscosity and relaxation time) of non-Newtonian fluids is still a technical challenge in spite of that various constitutive models such as Oldroyd-B model, Giesekus model, FENE-P model, etc., have been put forward.

To the best of authors' knowledge, most of the existing LES studies on the turbulent flow focus on the Newtonian fluid by applying the spatial SGS model, such as the Smagorinsky model [10]. Only few literature have been devoted to developing appropriate SGS models for the non-Newtonian turbulent flow. The representative literature are summarized as follows. Thais et al. [18] proposed to use a temporal LES (TLES) to study the polymer-induced turbulent drag-reducing channel flow using a temporal filter [19,20] and a temporal approximate deconvolution model (TADM) [21,22]. The representative simulation results were in good agreement with DNS results, indicating that TADM was an effective SGS model for polymer-induced non-Newtonian turbulent flow. Wang et al. [23] explored the approximate deconvolution model (ADM) and TADM, and found that TADM can offer more advantages over ADM in LES of non-Newtonian turbulent flow. In her work, TADM was applied to study the forced homogeneous isotropic turbulence (FHIT) with polymer additives and favorable numerical performances were achieved.

Li et al. [24] developed a mixed SGS model coupling a coherent-structure Smagorinsky model (CSM) and TADM, which was named as the mixed CSM and TADM (MCT) model. The cornerstone of MCT is to filter the continuity and momentum equations using the spatial CSM and filter the constitutive equation using the TADM, respectively. LES results of FHIT and turbulent drag-reducing channel flow demonstrated MCT is a successful mixed SGS model. To further improve the prediction accuracy of MCT, in 2017 Li et al. [25] improved the energy-decay suppression function of CSM and developed a mixed SGS model namely MICT (mixed ICSM and TADM), in which the improved CSM (ICSM) was used instead of the original CSM within MCT SGS model. According to the literature published in recent two years, the research on LES focuses on more wide turbulent types and engineering problems. For example, Ruettgers et al. [26] adopted the LES to investigate the turbulent flow over the DrivAer fastback vehicle, Lian et al. [27] performed the LES of turbulent flow over and through a rough permeable bed, and Chen et al. [28] studied the turbulent flow past stationary and oscillating square cylinders using LES. Evrim et al. [29] adopted the LES to simulate the turbulent thermal flow mixing in a vertical T-Junction configuration. Although above recent published literature have extended the LES to more wide application scopes, the turbulent flows in these studies are all Newtonian fluid.

In addition, for LES of non-Newtonian fluids only the single relaxation timescale constitutive model is considered in most scenarios. Rare work has been done on the hybrid SGS model for the non-Newtonian turbulent flow considering the multi-timescale constitutive model. Furthermore, the turbulent drag-reducing mechanism of turbulent flows at high-Reynolds-number is still open for discussion and gaps in the understanding persist, and the numerical performances of hybrid SGS model need to be further verified. Therefore, this paper will be devoted to carrying out numerical investigations of drag-reducing mechanism of high-Reynolds-number turbulent flow with surfactant additives using LES approach. The applications of hybrid SGS model, MICT, and multi-timescale constitutive model, N-parallel FENE-P model [30], are further investigated. Then drag-reducing mechanism is comprehensively explored from various aspects.

The structure of this work is organized as follows. In Section 2, the governing equations of LES, hybrid SGS model, and numerical methods are introduced. In Section 3, we validate the correctness of current LES method by commonly-used PIV experiments. The numerical cases at high Reynolds number with different solution concentrations are simulated and analyzed in Section 4. Summary and future work are presented in Section 5.

2 Governing Equations and Numerical Methods

In this study, the 3D incompressible single-phase turbulent drag-reducing channel flow is considered as the model problem, in which the turbulent drag reduction is induced by surfactant additives. The sketch map of computational domain and domain sizes along different directions are shown in Fig. 1.

2.1 LES Governing Equations

The governing equations of incompressible turbulent drag-reducing channel flow under isothermal condition include continuity equation, momentum equation and constitutive equation. To describe the rheological behaviors of non-Newtonian fluid with surfactant additives, the N-parallel FENE-P model proposed in [30] is adopted in this work. The core idea of N-parallel FENE-P model is to connect N FENE-P models with single relaxation time in parallel, then the stress-strain relation of different microstructures formed in non-Newtonian fluid can be modeled more truly compared with the traditional Giesekus model and FENE-P model with

single relaxation time. The N-parallel FENE-P model is capable to characterize the anisotropy of the relaxation-deformation of microstructures in non-Newtonian fluid and has been demonstrated a good prediction accuracy benefiting from the multiple relaxation timescales. Furthermore, for convenience of results discussion and to widen the application scope of our finding, here only the dimensionless form of governing equations are presented as follows, interested readers can refer to [24] for more details on the non-dimensionalization process, which are beyond the scope of present work.

$$\frac{\partial u_i^+}{\partial x_i^*} = 0 \tag{1}$$

$$\frac{\partial u_i^+}{\partial t^*} + u_j^+ \frac{\partial u_i^+}{\partial x_j^*} = \delta_{1i} - \frac{\partial p^{+'}}{\partial x_i^*} + \frac{1}{Re_\tau} \frac{\partial}{\partial x_j^*}\left(\frac{\partial u_i^+}{\partial x_j^*}\right) + \sum_{m=1}^{N} \frac{\beta_m}{We_{\tau,m}} \frac{\partial \left[f(r_m)\,c_{ij,m}^+\right]}{\partial x_j^*} \tag{2}$$

$$\frac{\partial c_{ij,m}^+}{\partial t^*} + u_k^+ \frac{\partial c_{ij,m}^+}{\partial x_k^*} - \frac{\partial u_i^+}{\partial x_k^*} c_{kj,m}^+ - \frac{\partial u_j^+}{\partial x_k^*} c_{ki,m}^+ = \frac{Re_\tau}{We_{\tau,m}} \left[\delta_{ij,m} - f(r_m)\,c_{ij,m}^+\right] \tag{3}$$

where the superscripts '$+, *$' denote the dimensionless variables; the nondimensional forms of main parameters are defined as: $x_i^* = \frac{x_i}{h}$, $t^* = \frac{t}{h/u_\tau}$, $u_i^+ = \frac{u_i}{u_\tau}$, $p^+ = \frac{p}{\rho u_\tau^2} = \frac{\bar{p}+p'}{\rho u_\tau^2} = \bar{p}^+ + p^{+'}$, where h denotes the half-height of channel and u_τ stands for the friction velocity, $u_\tau = \sqrt{\tau_w/\rho}$; the subscript i denotes the coordinates, $i = 1 \sim 3$; m denotes the mth FENE-P branch; N is the total number of FENE-P branch; β_m denotes the contribution of the mth FENE-P branch to the zero-shear viscosity of the flow; Re_τ stands for the friction Reynolds number, $Re_\tau = \rho\,u_\tau h/\eta_N$; $We_{\tau,m}$ denotes the Weissenberg number, $We_{\tau,m} = \lambda_m \rho u_\tau^2/\eta_N$; λ_m is the relaxation time of the mth FENE-P branch; $\bar{c}_{ij,m}^+$ denotes the component of conformation tensor; $f(r_m)$ is the non-linear stretching factor of the mth FENE-P branch, $f(r_m) = (L^2 - 3)/(L^2 - \text{trace}(\mathbf{c}_m^+))$; L is the maximum stretching length of the microstructures formed in non-Newtonian fluid.
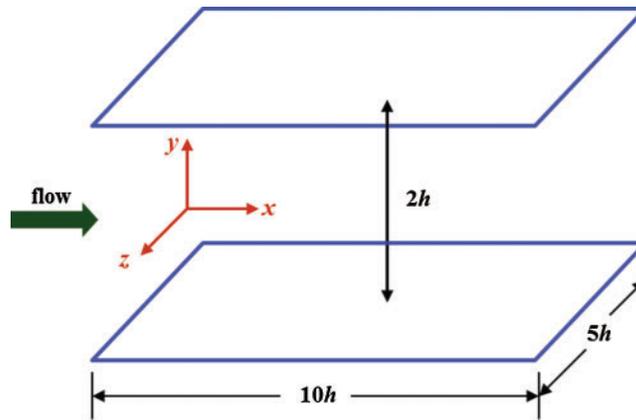

Figure 1: Sketch map of computational domain

To obtain the governing equations for LES, we need to filter the Eqs. (1)~(3) (filter the turbulent flow into a large scale part and a small scale part) using appropriate filters. In this

work, a non-uniform filter is used for equation filtering and a hybrid SGS model developed in [25] is used to close the filtered governing equations, in which the ICSM SGS model is applied to filter and close the momentum Eq. (2) and the TADM SGS model is used to filter and close the N-parallel FENE-P model Eq. (3), respectively. The filter operation yields following LES governing equations,

$$\frac{\partial \bar{u}_i^+}{\partial x_i^*} = 0 \tag{4}$$

$$\frac{\partial \bar{u}_i^+}{\partial t^*} + \bar{u}_j^+ \frac{\partial \bar{u}_i^+}{\partial x_j^*} = \delta_{1i} - \frac{\partial \bar{p}^{+'}}{\partial x_i^*} + \frac{1}{Re_\tau} \frac{\partial}{\partial x_j^*} \left(\frac{\partial \bar{u}_i^+}{\partial x_j^*} \right) + \sum_{m=1}^N \frac{\beta_m}{We_{\tau,m}} \frac{\partial \left[f(\bar{r}_m) \, \bar{c}_{ij,m}^+ \right]}{\partial x_j^*}$$

$$+ \sum_{m=1}^N \frac{\beta_m}{We_{\tau,m}} \frac{\partial R_{ij,m}}{\partial x_j^*} + \frac{\partial \tau_{ij}}{\partial x_j^*} \tag{5}$$

$$\frac{\partial \bar{c}_{ij,m}^+}{\partial t^*} + \bar{u}_k^+ \frac{\partial \bar{c}_{ij,m}^+}{\partial x_k^*} - \frac{\partial \bar{u}_i^+}{\partial x_k^*} \bar{c}_{kj,m}^+ - \frac{\partial \bar{u}_j^+}{\partial x_k^*} \bar{c}_{ki,m}^+ = \frac{Re_\tau}{We_{\tau,m}} \left[\delta_{ij,m} - f(\bar{r}_m) \, \bar{c}_{ij,m}^+ \right]$$

$$+ P_{ij,m} + Q_{ij,m} - \frac{Re_\tau}{We_{\tau,m}} R_{ij,m} + \chi_c \left(\bar{\gamma}_{ij,m} - \bar{c}_{ij,m}^+ \right) \tag{6}$$

where the bar '$-$' denotes the filter operation; τ_{ij} denotes the SGS stress of ICSM; $R_{ij,m}$ denotes the subfilter term concerning with the nonlinear restoring force; $P_{ij,m}$ and $Q_{ij,m}$ denote subfilter terms induced by the stretching of microstructures in non-Newtonian fluid; $\chi_c \left(\bar{\gamma}_{ij,m} - \bar{c}_{ij,m}^+ \right)$ is a regularization term standing for the kinetic energy transfers between the scales that cannot be recovered by the deconvolution procedure, $\chi_c = 1$ in this work. To close above LES governing equations, the periodic boundaries are set on streamwise (x) and spanwise (z) directions, and the no-slip boundary is imposed on the channel wall.

To model the SGS stress, in ICSM SGS model the traceless SGS stress tensor is defined by,

$$\tau_{ij}^a = \tau_{ij} - \frac{1}{3} \delta_{ij} \tau_{kk} = 2C \bar{\Delta} |\bar{S}| \bar{S}_{ij} \tag{7}$$

where $\bar{\Delta}$ is the filter width; $\bar{S}_{ij}$ is the filtered velocity-strain tensor, $\bar{S}_{ij} = \frac{1}{2} \left(\frac{\partial \bar{u}_j}{\partial x_i} + \frac{\partial \bar{u}_i}{\partial x_j} \right)$; C is the model parameter calculated by,

$$C = C_{\text{ICSM}} |F_{\text{CS}}|^{1.5} F_\Omega \tag{8}$$

where C_{ICSM} is a fixed model constant, C_{ICSM} is 1/16 for Newtonian fluid and 1/14 for non-Newtonian fluid, respectively; F_Ω denotes the energy-decay suppression function, $F_\Omega = 1 - |F_{\text{CS}}|$; F_{CS} stands for the coherent structure function defined as the second invariant $Q = -\frac{1}{2} \frac{\partial \bar{u}_j}{\partial x_i} \frac{\partial \bar{u}_i}{\partial x_j}$ normalized by the magnitude of a velocity gradient tensor $E = \frac{1}{2} \left(\frac{\partial \bar{u}_j}{\partial x_i} \right)^2$, $F_{\text{CS}} = \frac{Q}{E}$. To keep the model parameter C a small variance and be positive, $|F_{\text{CS}}| \leq 1$.

It should be mentioned the N-parallel FENE-P model is filtered on time domain, then the filter of variables in Eq. (6) reads,

$$\frac{\partial \bar{u}_i^{+(n+1)}}{\partial t^*} = \frac{\bar{u}_i^{+(n)} - \bar{u}_i^{+(n+1)}}{\Delta_u}, \quad 1 \le n \le \max(p, q) \tag{9}$$

$$\frac{\partial \bar{u}_i^*}{\partial t^*} = \frac{u_i - \bar{u}_i^*}{\Delta_u} \tag{10}$$

$$\frac{\partial \bar{c}_{ij,m}^{+(n+1)}}{\partial t^*} = \frac{\bar{c}_{ij,m}^{+(n)} - \bar{c}_{ij,m}^{+(n+1)}}{\Delta_c}, \quad 1 \le n \le \max(p, q) \tag{11}$$

$$\frac{\partial \bar{\phi}_{ij,m}}{\partial t^*} = \frac{\phi_{ij,m} - \bar{\phi}_{ij,m}}{\Delta_c} \tag{12}$$

$$\frac{\partial \bar{\gamma}_{ij,m}}{\partial t^*} = \frac{\gamma_{ij,m} - \bar{\gamma}_{ij,m}}{\Delta_c} \tag{13}$$

$$\frac{\partial}{\partial t^*} \left(\overline{\frac{\partial u_i^*}{\partial x_k^*} \phi_{kj,m}} \right) = \frac{1}{\Delta_c} \left(\frac{\partial u_i^*}{\partial x_k^*} \phi_{kj,m} - \overline{\frac{\partial u_i^*}{\partial x_k^*} \phi_{kj,m}} \right) \tag{14}$$

$$\frac{\partial}{\partial t^*} \left(\overline{\frac{\partial u_j^*}{\partial x_k^*} \phi_{ki,m}} \right) = \frac{1}{\Delta_c} \left(\frac{\partial u_j^*}{\partial x_k^*} \phi_{ki,m} - \overline{\frac{\partial u_j^*}{\partial x_k^*} \phi_{ki,m}} \right) \tag{15}$$

where Δ_u and Δ_c represent the temporal filter width of velocity and deformation rate, respectively; u_i^* denotes the deconvolution velocity, $u_i^* = \sum_{r=0}^{p} C_r \bar{u}_i^{+(r+1)}$; $\phi_{ij,m}$ and $\gamma_{ij,m}$ denote the deconvolution deformation rate, $\phi_{ij,m} = \sum_{r=0}^{p} C_r \bar{c}_{ij,m}^{+(r+1)}$, $\gamma_{ij,m} = \sum_{r=0}^{q} D_r \bar{c}_{ij,m}^{+(r+1)}$, where p and q denote the filtering times, in this work $p = 3$ and $q = 2$, C_r and D_r are deconvolution constant corresponding to p and q.

In Eqs. (5) and (6), the subfilter terms $P_{ij,m}$, $Q_{ij,m}$, $R_{ij,m}$ are unknown and should be calculated with the filtered variables following below formulas,

$$P_{ij,m} = \overline{\frac{\partial u_i^*}{\partial x_k^*} \phi_{kj,m}} - \frac{\partial \bar{u}_i^*}{\partial x_k^*} \bar{\phi}_{kj,m} \tag{16}$$

$$Q_{ij,m} = \overline{\frac{\partial u_j^*}{\partial x_k^*} \phi_{ki,m}} - \frac{\partial \bar{u}_j^*}{\partial x_k^*} \bar{\phi}_{ki,m} \tag{17}$$

$$R_{ij,m} = \overline{\left(f(r_m) \phi_{ij,m} - \delta_{ij} \right)} - \left(f(\bar{r}_m) \bar{\phi}_{ij,m} - \delta_{ij} \right) \tag{18}$$

2.2 Numerical Methods

In this part, the numerical methods used to solve LES governing equations are briefly introduced.

- **Discretization of computational domain.** In turbulent channel flow, the channel wall would exert great effects on flow development and flow properties (wall effect). In order to capture flow details accurately along the channel wall, in this work the uniform mesh is used in streamwise and spanwise directions while the non-uniform mesh is adopted in wall-normal direction, respectively. In this study, a mesh system with $32 \times 64 \times 32$ grid points is applied to discretize the 3D channel domain at the same time to save computation time and storage space, which has been verified by grid-independent solution [25].

- **Discretization of governing equations.** The LES governing equations can be discretized using pseudo-spectral method, finite difference method (FDM), finite volume method (FVM), etc. In this study, the commonly-used and easy-implemented FDM is applied. For the discretization of unsteady term, we use the Adams–Bashforth scheme, which is an explicit scheme with second-order accuracy. All diffusion terms are discretized by the second-order central difference scheme. In order to accurately solve the N-parallel FENE-P model and avoid overshoot/undershoot of conformation tensor, the high-resolution bounded scheme, MINMOD scheme [31], is adopted to discretize the convection terms of constitutive model. It should be mentioned that the staggered grid system is used in this study, where the pressure and conformation tensor are placed on the cell center and the velocity is placed on the cell face, respectively.

- **Solver.** Compared with the simulation of laminar flow, it requires much longer time and more computing resources to simulate the turbulent flow. Therefore, the time consumption of DNS or LES is always unfavorable or sometimes is unacceptable in engineering community. In order to speed-up the computation, the multigrid method [32] is applied to solve the discrete LES governing equations in present work.

- **Algorithm.** To decouple the pressure and velocity in LES of turbulent flow, the projection algorithm is applied in this work. The cornerstone of projection algorithm in solving LES governing equations is stated as follows: first construct and implicitly solve the pressure fluctuation equation, then solve momentum equations in two steps: the first step is to solve the momentum equations without the gradient term of pressure fluctuation explicitly, and then the intermediate velocity can be obtained; the second step is to substitute the intermediate velocity into the pressure fluctuation equation, then we get the full velocity. Based on the obtained pressure fluctuation and velocity, the N-parallel FENE-P model can be solved explicitly.

3 Validation Using PIV Experiment

In this work, the LES of turbulent drag-reducing channel flow with surfactant additives is carried out using in-house FORTRAN code. Before LES, first the correctness and reliability of in-house code results are validated by the PIV experiment, which plays a significant role in the visualization and measurement of flow field (others include laser doppler velocimetry (LDV), stereoscopic PIV (SPIV), planar laser-induced fluorescence (PLIF), etc.). A large body of literature have reported this mature technique, readers of interest can refer to [33] for more details of PIV. Here, only the experimental apparatus and experimental parameters used in this work are briefly introduced.

3.1 Experimental Apparatus

The PIV experimental system used in this study is composed of a channel flow part and a PIV measurement part.

3.1.1 Channel Flow System

Fig. 2 shows the channel flow system which mainly consists of a transparent 3D channel, three tanks, a pump, a flow meter, a honeycomb rectifier, etc. In this system, the working fluid is circulated in the closed-circuit loop and is heated to the required temperature to provide a developed and stable turbulent drag-reducing flow. More specifically, water, tracer particles, and surfactant additives can be added and supplemented into the circulating system through tank A and are well mixed by the agitator. The temperature of the whole flow system is keep constant by a heater in tank A. With the tank B, the surfactant solution can steadily flow into the channel. The function of honeycomb rectifier installed at the right side of tank B is to destroy large turbulent vortex structures and remove all the bubbles in the loop to yield a well-developed turbulent flow in front of the measure window. The bulk flow rate can be measured by the flow meter and the adjustable frequency pump is set to the required working condition. The sizes of transparent channel along x, y and z directions are 4500 mm, 40 mm and 500 mm, respectively. As shown in Fig. 2, there is a removable measure window located at the channel wall, the center of which is 3650 mm away from the channel entrance. Along the upstream and downstream of the measure window, there are two ports used to measure and monitor the pressure difference.
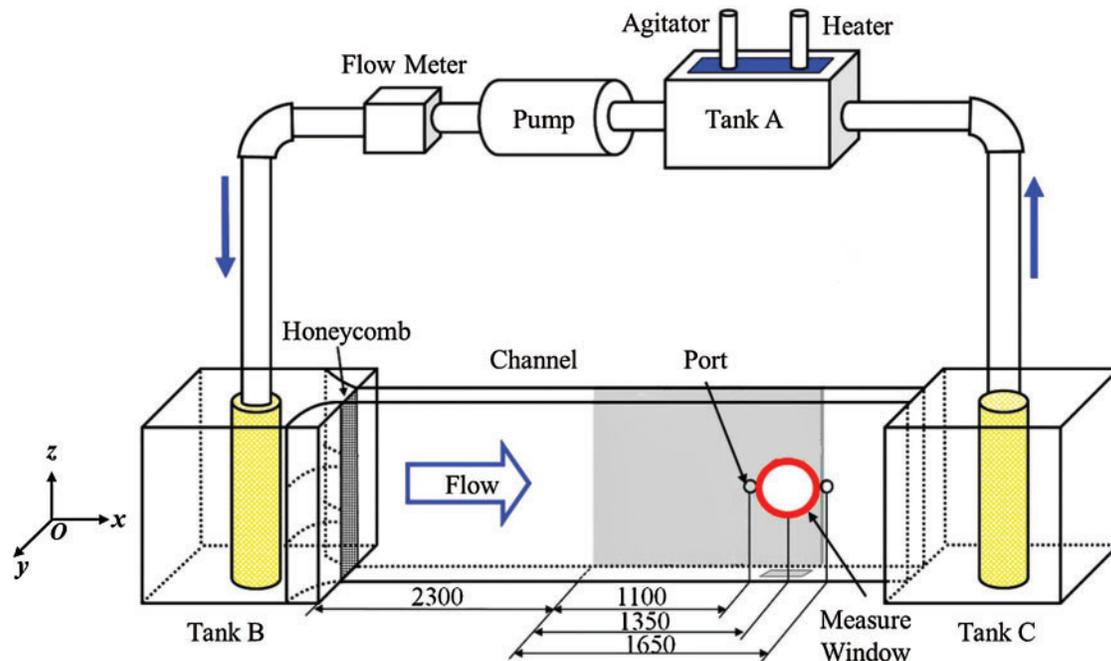

Figure 2: Sketch map of channel flow system (unit:mm)

3.1.2 PIV Measurement System

Fig. 3 displays the PIV system adopted to measure turbulent flow fields in a x–y plane, it is composed of a synchronization device, a double-pulse Nd: YAG Laser, a charge-couple device

(CCD) camera and a computer with the image processing and analysis software, etc. The basic principle is that the light scattered by tracer particles is acquired and the moving trajectory frames of tracer particles are recorded. Then the PIV images of turbulent flow fields are analyzed using the cross-correlation technique, which relies on two consecutive frames obtained during a period between laser pulses. Note that in the image acquisition process, the CCD camera and YAG Laser should be controlled by the synchronization device to avoid mismatch.
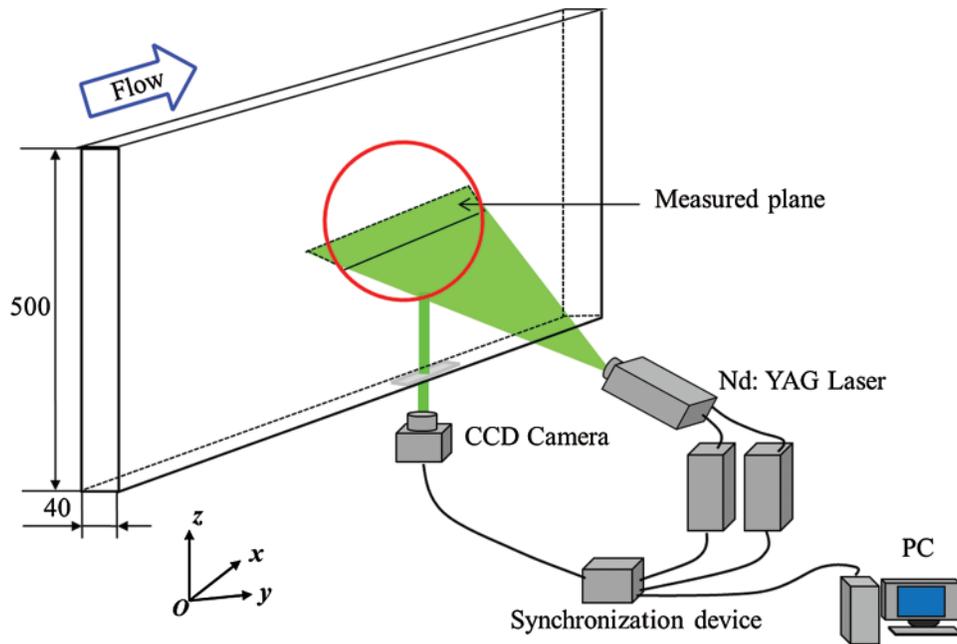

Figure 3: Sketch map of particle image velocimetry measurement system (unit:mm)

It should be mentioned that to reduce the uncertainty factors in PIV measurement, the standard calibration board should be used to calibrate the focal length of CCD camera. In addition, it is also significant to select appropriate tracer particles because the quality of acquired flow field images and the accuracy of the measurement heavily depend on tracer particles. Generally, the tracer particle should possess good following performance and light-reflection property. In this work, we use a polyethylene powder named UF-20S as the tracer particle, the density is 0.92 g/cm^3 that is approximate to water with good following performance and the mean diameter is 20 μm that offers good light-reflection property.

3.2 Experimental Parameters

In our PIV experiment, a cationic surfactant, Cetyltrimethyl Ammonium Chloride (CTAC), is selected as the turbulent drag reducer. The chemical formula of CTAC is $C_{16}H_{33}N(CH_3)_3Cl$ and the molecular weight is 320. To maintain the stability of microstructures formed in CTAC solution, the Sodium Salicylate (NaSal) with same weight concentration is added into CTAC solution to provide counter ions, whose chemical formula is $C_7H_5O_3Na$ with the molecular weight of 160. During the PIV measurement, the weight concentration of CTAC/NaSal solution is fixed at 60 ppm and the temperature of CTAC/NaSal solution is maintained at 298 K, the purpose of this setting is to produce a stable experimental results in the channel flow. The measured zone is

a x–y plane at the channel center with the size of 48 mm × 40 mm. In this work, 500 images of the instantaneous turbulent flow velocity fields were acquired with a time interval of 1000 μs between two laser pluses for each case. The frequency of photograph acquisition is set as 5 Hz.

In order to make the LES results be comparable with PIV experimental data, the calculation parameters of LES should be set properly and carefully. In this work, a double-parallel FENE-P model proposed in [30] is applied to describe rheological behaviors of the CTAC/NaSal solution. Through the channel flow system, the bulk Reynolds number is adjusted to approximate 1.5×10^4, thus the friction Reynolds number can be set about 300 in LES. It should be noted that it is difficult to accurately measure the apparent viscosity of 60 ppm CTAC/NaSal solution by the rheometer due to the tiny difference of apparent viscosity between 60 ppm CTAC/NaSal solution and water, thus it can be inferred that the apparent viscosity of CTAC/NaSal solution is almost same as that of water. It is also reported that the measured relaxation time of CTAC/NaSal solutions with the weight concentration less than 75 ppm was in the range of 0.1~0.4 s under the temperature of 290~301 K. By comparing the experimental conditions with the work of Li et al. [34], we found the relaxation time of CTAC/NaSal surfactant solution with similar weight concentration is around 0.3 s. Thus, in this work the Weissenberg number We_τ is calculated to be around 40.

3.3 Results Comparison

In this part, PIV measured results are compared with those simulated by LES. Note that in the PIV experiment only two-dimensional flow fields in x–y plane were measured, thus the full details of turbulent flow characteristics cannot be obtained. Here, part of representative measured results such as streamwise mean velocity, wall-normal velocity fluctuation, and Reynolds shear stress are displayed and compared, as shown in Fig. 4.

Fig. 4a presents the comparison of dimensionless streamwise mean velocity obtained by PIV and LES. It can be clearly observed that overall the LES result can match with that of PIV result. In the logarithmic layer and channel center, the PIV result is slightly larger than that of LES. Although this small deviation exists between the PIV result and LES result, it can be acceptable from the perspective of engineering. In Fig. 4b, the root-mean-square (RMS) of dimensionless wall-normal velocity fluctuation of PIV experiment and LES are compared in detail. From the comparison it can be seen that the LES result is a little larger than that of PIV in logarithmic layer and main flow region. However, the variation trend of RMS of dimensionless wall-normal velocity fluctuation obtained by these two methods are almost same with each other, and the peak positions of the two dimensionless wall-normal velocity fluctuation RMS are same, too. It indicates the LES approach used in this study is capable of predicting the turbulent drag-reducing flow accurately. Fig. 4c compares the dimensionless Reynolds shear stress calculated by LES and measured by PIV experiment. Overall, the LES result can match with the PIV measured result despite that the simulated Reynolds shear stress is slightly larger than the measured one in logarithmic layer. The peak positions of Reynolds shear stress obtained by LES and PIV are same with each other.

From above comparisons, it can be concluded that the results of LES can match with measured results of PIV experiment overall, and the deviations only exist at some specific locations. The main reasons for these deviations can be attributed to: (1) The parameter settings of LES cannot be guaranteed all same with PIV experimental conditions. As mentioned in last subsection, it is difficult to measure the apparent viscosity and relaxation time of 60 ppm CTAC/NaSal solution accurately, thus there would be some errors for the Weissenberg number

We_τ and viscosity ratio $\beta_1 + \beta_2$ used in LES compared with the real condition in PIV experiment. Such errors between simulation parameters and experimental parameters will introduce deviations between LES simulation results and experimental results; (2) Compared with DNS, in LES the turbulent flow is first filtered and then only the large scale vortex structures are simulated by solving the filtered equations but the small scale vortex structures are solved using subgrid scale models. Due to that different SGS models can offer different prediction accuracies, the LES itself would introduce numerical errors to a certain degree depending on the selection of SGS model. In conclusion, it is reasonable that some deviations exist between LES results and PIV results.
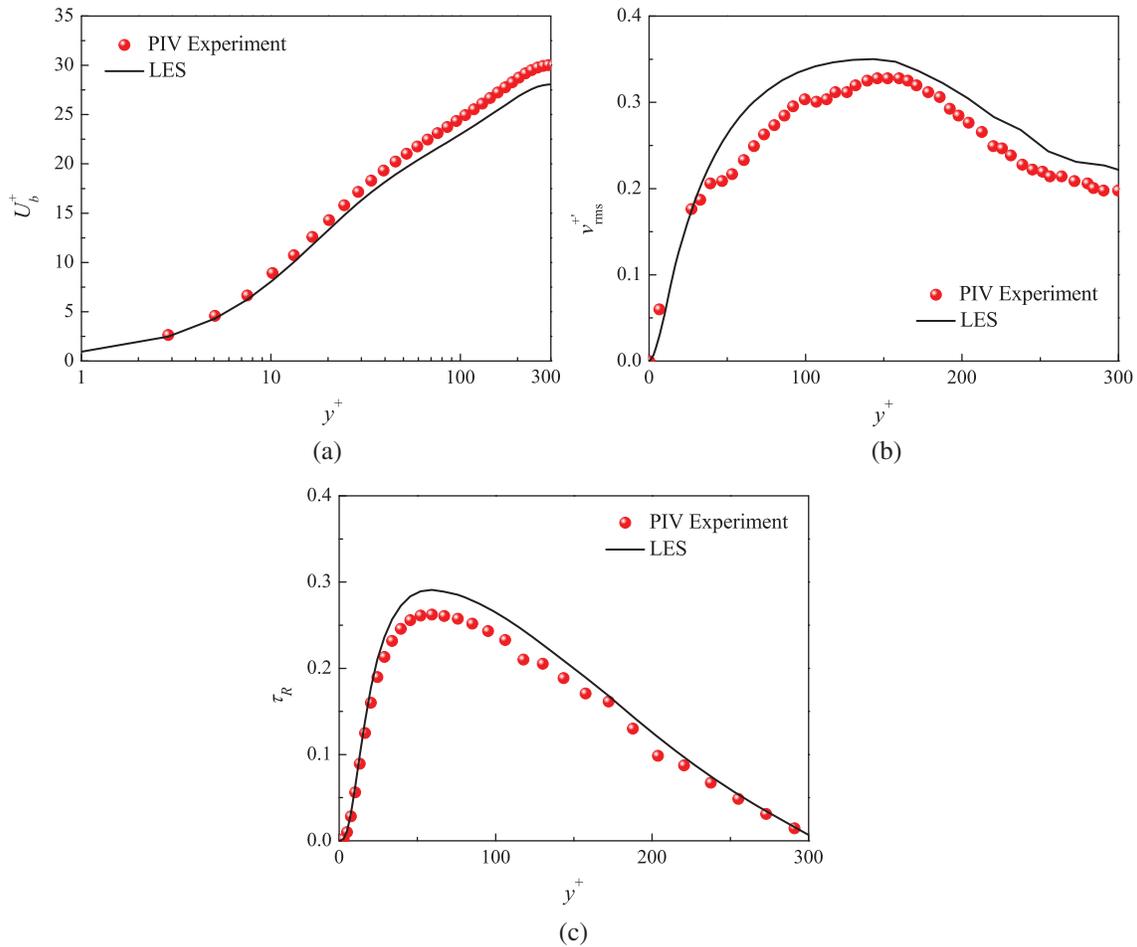

Figure 4: Comparison of LES results and PIV results. (a) Streamwise mean velocity. (b) RMS of wall-normal velocity fluctuations. (c) Reynolds shear stress

4 Case Studies and Results

4.1 Case Description

In this part, we investigate the drag-reducing mechanism of high-Reynolds-number turbulent channel flow with surfactant additives using the verified LES method through seven numerical

cases, among which the case C0 is a Newtonian turbulent flow used for comparison and cases C1~C6 are non-Newtonian turbulent flow with surfactant additives. In these cases the double-parallel FENE-P model ($L = 100$) is adopted to describe non-Newtonian fluid properties and the friction Reynolds number is set as 600, the other parameter settings are presented in Tab. 1. In the simulation, a $32 \times 64 \times 32$ mesh system is applied and the grid independence test can refer to [18,24,25]. For the hybrid SGS model used in LES, the width for spatial filter is set as 0.0634, and the width for temporal filter of both velocity and conformation tensor is set as $10\Delta t^*$.

Table 1: Simulation parameters setting for cases C0~C6

Case	Δt^*	$We_{\tau,1}$	β_1	$We_{\tau,2}$	β_2
C0	5×10^{-4}	–	–	–	–
C1	1×10^{-4}	10	0.1	10	0.1
C2	1×10^{-4}	20	0.1	20	0.1
C3	1×10^{-4}	30	0.1	30	0.1
C4	1×10^{-4}	40	0.1	40	0.1
C5	1×10^{-4}	20	0.15	20	0.15
C6	1×10^{-4}	20	0.2	20	0.2

It should be noted that the initial conditions should be given in this unsteady turbulent flow simulation, which are shown below,

$$\bar{u}^+ \left(0, x^*, y^*, z^*\right) = \bar{u}^{+(2)} \left(0, x^*, y^*, z^*\right) = \bar{u}^{+(3)} \left(0, x^*, y^*, z^*\right) = \bar{u}^{+(4)} \left(0, x^*, y^*, z^*\right) = u^+ \left(0, x^*, y^*, z^*\right)$$
(19)

$$\bar{v}^+ \left(0, x^*, y^*, z^*\right) = \bar{w}^+ \left(0, x^*, y^*, z^*\right) = u^+ \left(0, x^*, y^*, z^*\right), \overline{u_i^* u_j^*} \left(0, x^*, y^*, z^*\right) = u_i^+ u_j^+ \left(0, x^*, y^*, z^*\right) \quad (20)$$

$$\bar{c}_{ij}^+ \left(0, x^*, y^*, z^*\right) = \bar{c}_{ij}^{+(2)} \left(0, x^*, y^*, z^*\right) = \bar{c}_{ij}^{+(3)} \left(0, x^*, y^*, z^*\right) = \bar{c}_{ij}^{+(4)} \left(0, x^*, y^*, z^*\right) = c_{ij}^+ \left(0, x^*, y^*, z^*\right) \quad (21)$$

$$\bar{\phi}_{ij} \left(0, x^*, y^*, z^*\right) = \bar{\gamma}_{ij} \left(0, x^*, y^*, z^*\right) = \bar{c}_{ij}^+ \left(0, x^*, y^*, z^*\right)$$
(22)

4.2 Results Discussion
4.2.1 Turbulent Drag Reduction Rate
First the drag reduction (DR) rate of cases C0~C6 is presented in Tab. 2, which is defined as,

$$\text{DR} = \frac{C_f^D - C_f}{C_f^D} \times 100\%$$
(23)

where C_f denotes the Fanning friction coefficient of the surfactant solution, $C_f = 2/\left(U_b^+\right)^2$, U_b^+ is the dimensionless streamwise mean velocity; C_f^D represents the Fanning friction coefficient of the Newtonian flow, $C_f^D = 0.073 Re_b^{-0.25}$, Re_b is the bulk Reynolds number, $Re_b = 2 Re_\tau U_b^+$.

From Tab. 2, it can be obviously seen that a good turbulent drag reduction is obtained in this study. For example, in case C1 with small We_τ and β the DR is up to 51.07%. We can also observe that in cases C1~C4, the effect of Weissenberg number is not so strong compared with the turbulent flow at low Reynolds number, where with the increase of Weissenberg number, the DR increases with the same trend. The main reason is that in high-Reynolds-number turbulent flows, the DR depends not only on Weissenberg number, but also on the ratio of Weissenberg number to friction Reynolds number. It means that the effect of Weissenberg number is suppressed in high-Reynolds-number turbulent flows. Similarly, cases C5 and C6 also illustrate the effect of concentration is not always positive, actually the solution concentration has dual effects on DR rate. In our studied cases, with the increase of solution concentrations, the DR rate will first increase and then decrease. The reason for this interesting phenomenon can be explained as follows: when the solution concentration increases (more surfactant is added into the solution), more microstructures are formed in the surfactant solution, then much stronger elastic drag would be introduced. When the introduced elastic drag is larger than the reduced flow drag, the overall DR rate will decrease. Therefore, when the solution concentration exceeds a threshold, the DR rate will decrease with the increase of solution concentration.

Table 2: Turbulent drag reduction rate of cases C0~C6

Case	C0	C1	C2	C3	C4	C5	C6
DR(%)	0	51.07	51.91	53.60	54.52	49.65	45.49

4.3 Streamwise Mean Velocity

The mean velocity along streamwise direction is a main flow field characteristic in the turbulent drag-reducing flow. Fig. 5 displays variations of dimensionless streamwise mean velocity U_b^+ with y^+, where the dimensionless streamwise mean velocity is defined as $U_b^+ = U_b/u_\tau$ (U_b is the streamwise mean velocity) and y^+ is defined as $y^+ = \rho y u_\tau/\eta$, respectively. From Fig. 5 it can be seen that there are some distinctions in the dimensionless streamwise mean velocity for the turbulent drag-reducing flow and Newtonian turbulent flow. In viscous sublayer, both U_b^+ and its gradient of turbulent drag-reducing flow are smaller than those of Newtonian turbulent flow. It indicates the surfactant additives change the distributions of U_b^+ and its gradient in viscous sublayer. In transition layer, compared with the Newtonian turbulent flow, both the gradient of U_b^+ and the thickness of transition layer increase in the turbulent drag-reducing flow. In logarithmic layer and main flow region, U_b^+ and its gradient of turbulent drag-reducing flow are larger than those of Newtonian turbulent flow. Furthermore, with increase of the elastic effect (concentration), the difference in U_b^+ and its gradient between the surfactant-turbulent flow and the Newtonian turbulent flow becomes more obvious.

4.3.1 Deformation Rate

The elasticity strength of turbulent flow with surfactant additives can be characterized by the dimensionless RMS of deformation rate fluctuation of microstructures formed in surfactant

solution. Compared with the diagonal component of conformation tensor, $\bar{c}_{xx}^{+}$, the fluctuations of other components of conformation tensor is very small, thus the $\bar{c}_{xx}^{+\prime}$ plays dominant role in the deformation of microstructures in surfactant solutions. Fig. 6 presents the profiles of RMS of $\bar{c}_{xx}^{+\prime}$ with y^{+}, in which the curve with dramatic change part is enlarged.
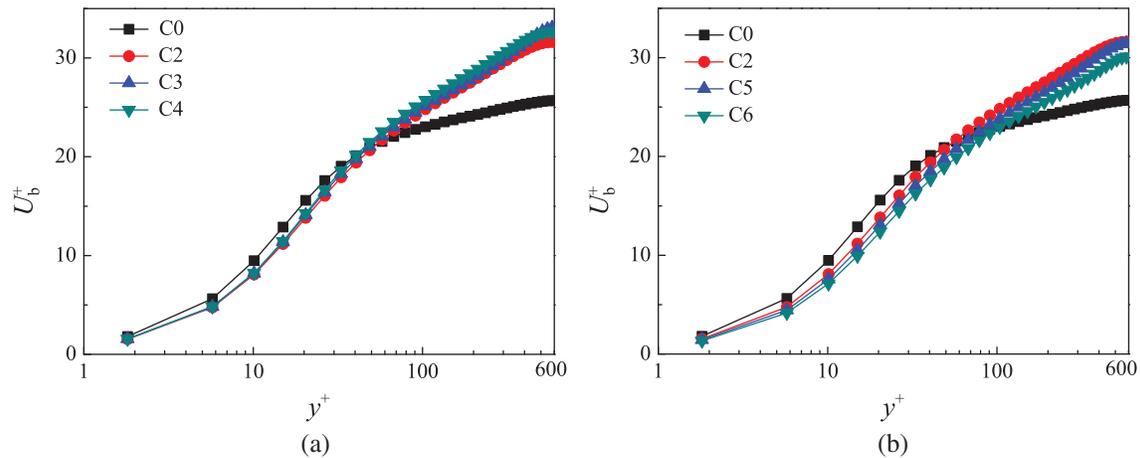

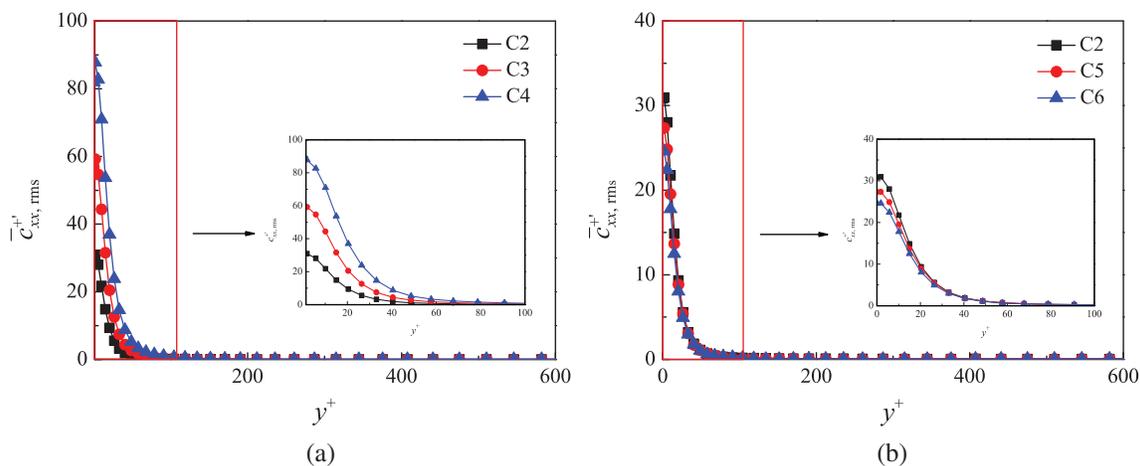**Figure 5:** Dimensionless streamwise mean velocity profiles. (a) Different We_τ in different cases. (b) Different β in different cases

Figure 6: Profiles of root-mean-square of $\bar{c}_{xx}^{+\prime}$ with y^{+}. (a) Different We_τ in different cases. (b) Different β in different cases

From Fig. 6, it is clear to see that more closer near the channel wall, much more larger the $\bar{c}_{xx}^{+\prime}$ is, and the maximum value of $\bar{c}_{xx}^{+\prime}$ is achieved on the channel wall. This is because near the channel wall the shear stress is much stronger than that in the channel center. Meanwhile, it demonstrates that the influencing zone of surfactant additives in turbulent flows is the near-wall region, the viscoelasticity exerts great effects on the viscous sublayer and transition layer near the channel wall. It is also worth noting that the numerical instability of LES of turbulent

drag-reducing flow mainly attributes to the fluctuation of deformation rate. To vividly visualize the distribution of $\bar{c}_{xx}^{+'}$, the contour of $\bar{c}_{xx}^{+'}$ in x^*-y^* plane located at channel center of cases C2 and C4 is presented in Fig. 7. We can see that the two-dimensional distribution of $\bar{c}_{xx}^{+'}$ agrees with the profiles of $\bar{c}_{xx}^{+'}$ along wall-normal direction. In addition, with the increase of surfactant concentration, the deformation of microstructures in turbulent drag-reducing flow becomes stronger and thus $\bar{c}_{xx}^{+'}$ increases.
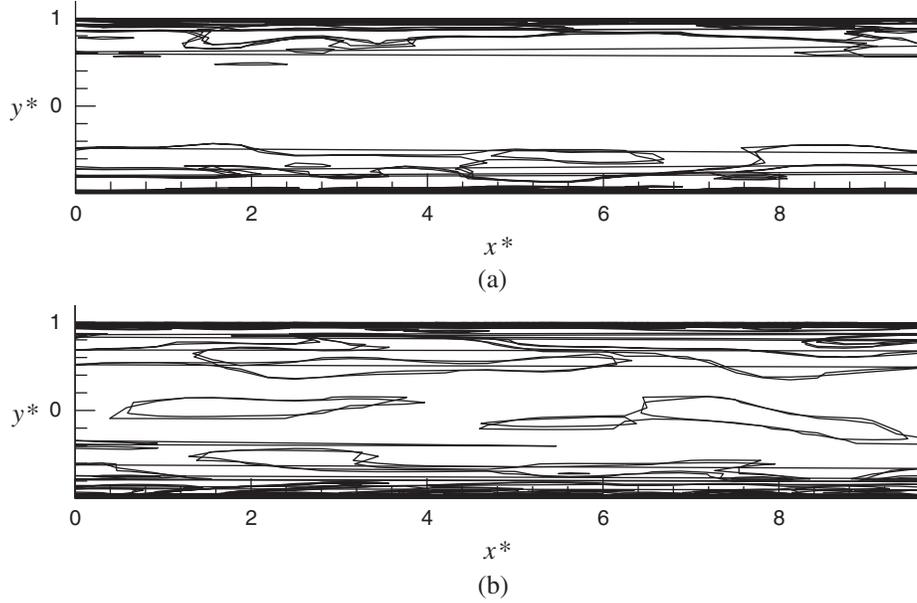

Figure 7: Distributions of $\bar{c}_{xx}^{+'}$ in x^*-y^* plane. (a) Case C2. (b) Case C4

4.3.2 Shear Stress

One reason for the drag reduction in turbulent flow is that the surfactant additives in turbulence change the balance of shear stress and lead to the redistribution of shear stress. Therefore, it is essential to analyze different shear stresses in turbulent flow, as shown in formula (24),

$$\tau_{\text{total}} = \tau_R + \tau_V + \tau_E = -\left\langle \bar{u}^{+'} \bar{v}^{+'} \right\rangle + \frac{1}{Re_\tau} \frac{\partial U_b^+}{\partial y^*} + \sum_{m=1}^{N} \frac{\beta_m}{We_{\tau,m}} f(\bar{r}_m) \bar{c}_{xy,m}^+ \tag{24}$$

where τ_{total} stands for the total shear stress; $\tau_R = -\left\langle \bar{u}^{+'} \bar{v}^{+'} \right\rangle$ represents the Reynolds shear stress; $\tau_V = \frac{1}{Re_\tau} \frac{\partial U_b^+}{\partial y^*}$ denotes the viscous shear stress; $\tau_E = \sum_{m=1}^{N} \frac{\beta_m}{We_{\tau,m}} f(\bar{r}_m) \bar{c}_{xy,m}^+$ denotes the elastic shear stress.

Fig. 8 depicts the profiles of three different shear stresses with y^+ regarding cases C0, C2~C4. From Fig. 8, it can be concluded that the surfactant additives substantially change the balance of shear stresses in turbulent drag-reducing flow. In the near-wall region, the τ_R in Newtonian turbulent flow is much larger than that in turbulent drag-reducing flow, the peak value is around two times of that in turbulent drag-reducing flow. This is also the main reason

why the friction drag of Newtonian turbulent is far larger than that of turbulent drag-reducing flow. Furthermore, the peak position of τ_R curve in turbulent drag-reducing flow moves towards the main flow region, corresponding to the increase of transition layer thickness. Similar to the Newtonian turbulent flow, the influencing zone of τ_V in turbulent drag-reducing flow is the near-wall region. It decreases quickly when moving away from the near-wall region. One small distinction is that τ_V in turbulent drag-reducing flow is little stronger than that in Newtonian turbulent flow. Different from the low-Reynolds-number turbulent drag-reducing flow, the peak of τ_E curve in the near-wall region cannot be observed clearly. In turbulent drag-reducing flow, the existence of τ_E, the decrease of τ_V and τ_R finally reduce the frictional resistance in channel wall and induce the drag reduction.
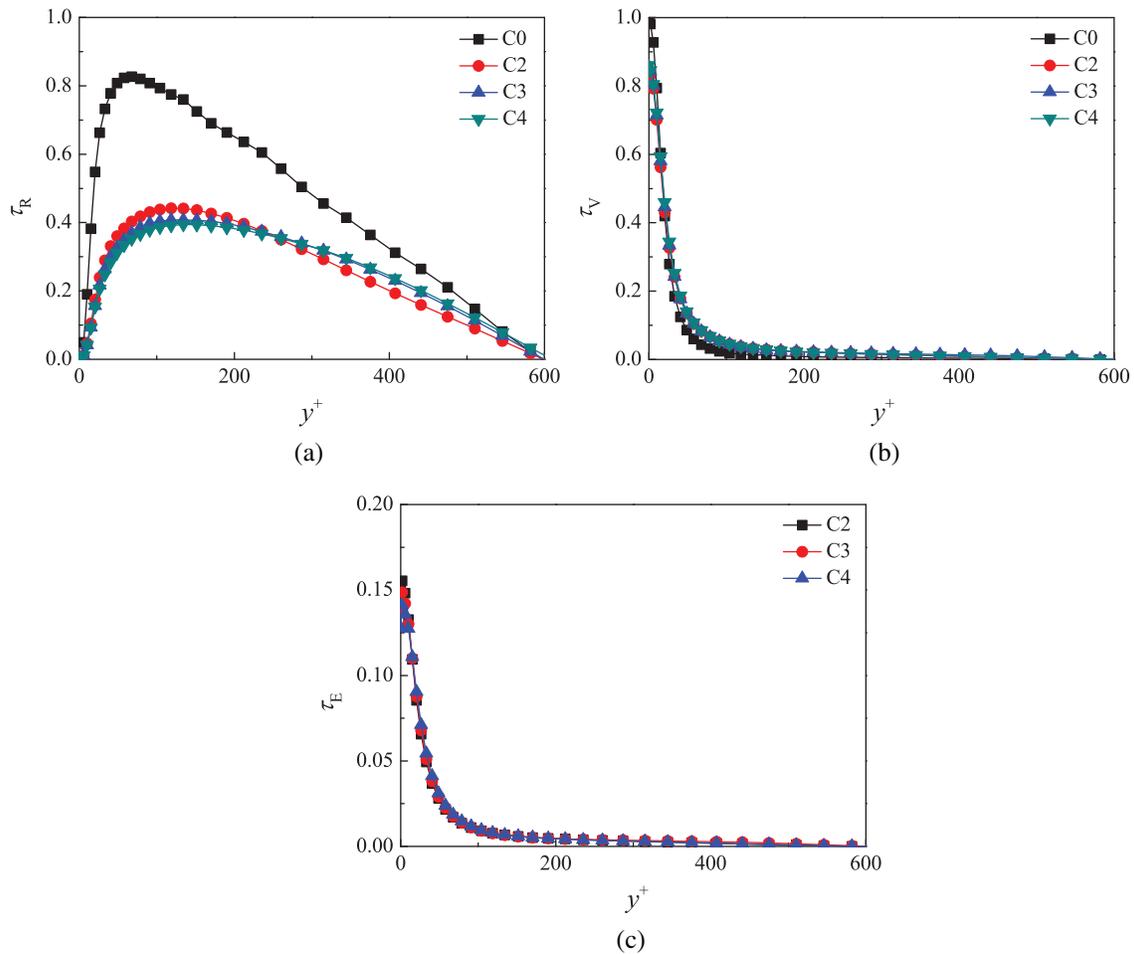

Figure 8: Profiles of different shear stresses with y^+. (a) Reynolds shear stress. (b) Viscous shear stress. (c) Elastic shear stress

4.3.3 Transport and Dissipation of Turbulent Kinetic Energy

Compared with Newtonian fluid, the elastic effect of turbulent drag-reducing flow induced by the surfactant drag reducer changes the transport and dissipation of turbulent kinetic energy

(TKE). To investigate the production, transport and dissipation of TKE as well as their relation with the drag-reducing mechanism, here the TKE transport equation is presented below,

$$\frac{D}{Dt}\left\langle \bar{u}_i^{+\prime} \bar{u}_j^{+\prime} \right\rangle = P_{K,ij} + D_{V,ij} + D_{T,ij} + \varepsilon_{K,ij} + D_{P,ij} + \varepsilon_{E,ij} \tag{25}$$

where $P_{K,ij}$ denotes the TKE production, $P_{K,ij} = -\left\langle \bar{u}_j^{+\prime} \bar{u}_k^{+\prime} \frac{\partial \bar{U}_i^+}{\partial x_k^*} + \bar{u}_i^{+\prime} \bar{u}_k^{+\prime} \frac{\partial \bar{U}_j^+}{\partial x_k^*} \right\rangle$; $D_{V,ij}$ denotes the viscous diffusion, $D_{V,ij} = \frac{1}{Re_\tau} \frac{\partial^2 \left\langle \bar{u}_i^{+\prime} \bar{u}_j^{+\prime} \right\rangle}{\partial x_k^{*2}}$; $D_{T,ij}$ denotes the turbulent diffusion, $D_{T,ij} = -\frac{\partial}{\partial x_k^*} \left\langle \bar{u}_i^{+\prime} \bar{u}_j^{+\prime} \bar{u}_k^{+\prime} \right\rangle$; $\varepsilon_{K,ij}$ represents the TKE dissipation, $\varepsilon_{K,ij} = \frac{2}{Re_\tau} \left\langle \frac{\partial \bar{u}_i^{+\prime}}{\partial x_k^*} \frac{\partial \bar{u}_j^{+\prime}}{\partial x_k^*} \right\rangle$; $D_{P,ij}$ indicates the pressure diffusion, $D_{P,ij} = -\left\langle \bar{u}_j^{+\prime} \frac{\partial \bar{p}^{+\prime}}{\partial x_i^*} + \bar{u}_i^{+\prime} \frac{\partial \bar{p}^{+\prime}}{\partial x_j^*} \right\rangle$; $\varepsilon_{E,ij}$ denotes the elastic dissipation,

$$\varepsilon_{E,ij} = \sum_{m=1}^{N} \frac{\beta_m}{We_{\tau,m}} \left\langle \bar{u}_i^{+\prime} \frac{\partial \left(f(\bar{r}_m) \bar{c}_{jk,m}^+ \right)}{\partial x_k^*} + \bar{u}_j^{+\prime} \frac{\partial \left(f(\bar{r}_m) \bar{c}_{ik,m}^+ \right)}{\partial x_k^*} \right\rangle,$$ this term doesn't exist in the Newtonian turbulent flow.

As shown in Fig. 9, the profiles of different terms related with the production, transport and dissipation of TKE mentioned in Eq. (25) are presented. From Fig. 9a, we can see that the TKE production in turbulent drag-reducing flow is far smaller than that in Newtonian turbulent flow, the peak value of P_K is only 30% of that in Newtonian turbulent flow. The reason for the dramatic drop of P_K can be attributed to the decrease of Reynolds shear stress in turbulent drag-reducing flow. Fig. 9b indicates that no matter for the Newtonian turbulent flow or the turbulent drag-reducing flow, the influencing zone of viscous diffusion focuses on the near-wall region. In transition layer, the viscous diffusion achieves the minimum value, which means the energy dissipation induced by viscous diffusion is maximum. In the main flow region, the viscous diffusion can be neglected. The peak value of D_V in turbulent drag-reducing flow is reduced obviously compared with that in Newtonian turbulent flow. From Fig. 9c, it can be observed that the turbulent diffusion in Newtonian turbulent flow is stronger in the near-wall region than that in turbulent drag-reducing flow. In turbulent flow with surfactant, the turbulent diffusion tends to be stable after the negative peak, it implies the turbulent fluctuation is suppressed and reduced in turbulent drag-reducing flow, the turbulent fluctuations and fluctuation kinetic energy decrease gradually and tend to be stable. Fig. 9d demonstrates the profile of TKE dissipation along the wall-normal direction. It can be observed that no matter in Newtonian turbulent flow or in turbulent drag-reducing flow, ε_K is always negative, which means the turbulent kinetic energy is dissipated. The ε_K is large in the near-wall region and is reduced away from the channel wall. Furthermore, ε_K in turbulent drag-reducing flow is smaller than that in Newtonian turbulent flow because the viscoelasticity changes the transport of TKE and thus the dissipation of TKE is suppressed and reduced. From Fig. 9e, it can be found the variation trend of pressure diffusion is similar to that of turbulent diffusion. Fig. 9f shows the elastic dissipation profile, which only exists in turbulent drag-reducing flow with non-Newtonian fluid (surfactant solution in this work). From Fig. 9f, we see that the elastic dissipation is relatively small, and the peak of elastic dissipation exists in the transition layer of turbulent drag-reducing flow. It indicates the elastic energy mainly dissipates in transition layer and contributes to the increase of thickness of transition layer.
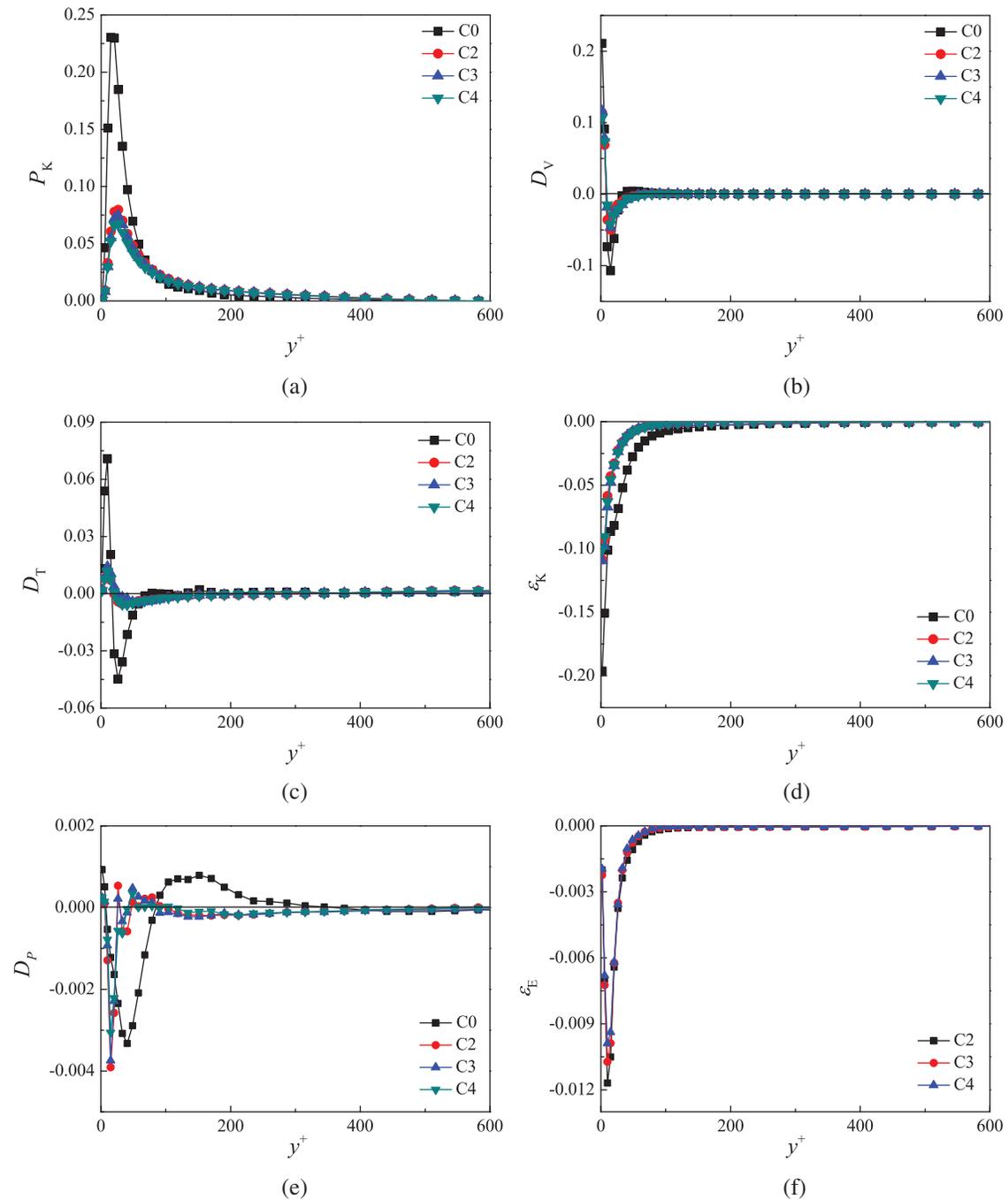
Figure 9: Analysis on the balance of turbulent kinetic energy. (a) Production of TKE. (b) Viscous diffusion. (c) Turbulent diffusion. (d) Dissipation of TKE. (e) Pressure diffusion. (f) Elastic dissipation

Based on above analyses, we can conclude that compared with Newtonian turbulent flow, the addition of surfactant drag reducers to the turbulent flow obviously changes the production, transport and dissipation of TKE. Especially, the surfactant additives mainly affect the TKE in

the near-wall region but has little influence on the main flow region. The reduction of turbulent drag has close relation with the dramatic decrease of production of TKE.
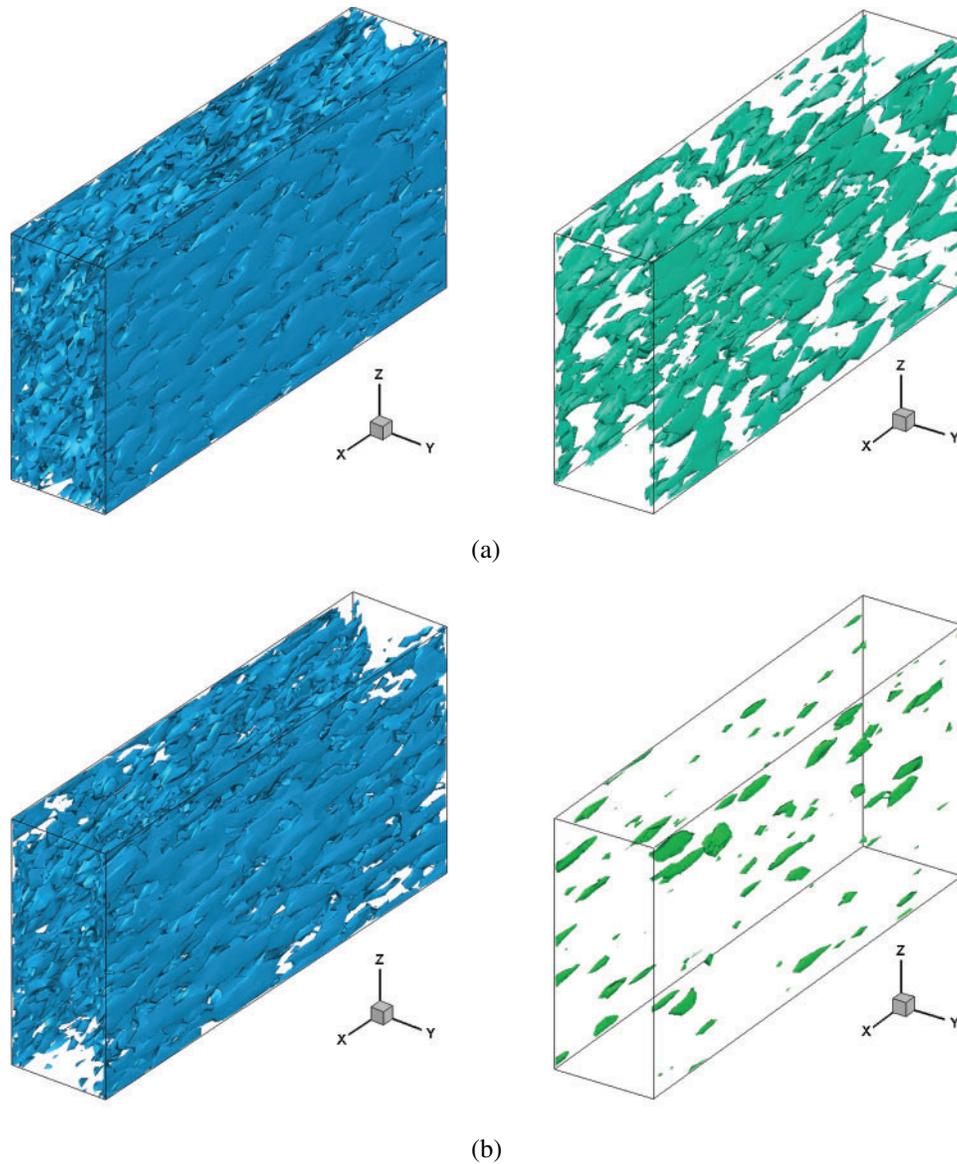

(a)

(b)

Figure 10: Comparison of coherent structures of C0 (left) and C2 (right). (a) $Q = 50$. (b) $Q = 250$

4.3.4 Coherent Structures

To reveal the underlying drag-reducing mechanism, the relation between drag reduction and coherent structures is discussed here. Fig. 10 shows the turbulent coherent structures of C0 (Newtonian fluid) and C2 (non-Newtonian fluid with surfactant) with $Q = 50$ and $Q = 250$, where the vortex tube structures exist when $Q > 0$ according to the Q method [35]. From Fig. 10, it can be clearly observed that with the same Q value, the number of vortex tube structures

in Newtonian turbulent flow is much more than that in non-Newtonian turbulent flow. This phenomenon indicates that the surfactant additives can substantially suppress the formation of turbulent coherent structures in high-Reynolds-number turbulent channel flow. Thus after the surfactant is added into the turbulent flow, the intermittency of turbulent flow is suppressed and the frequency and intensity of turbulent burst events are reduced and weakened appreciably. With the increase of Q value, the number of coherent structures decreases both in Newtonian and in non-Newtonian turbulent flows.

4.3.5 Skewness Factor and Flatness Factor

To quantitatively clarify that the intermittency of turbulent flow is suppressed by the surfactant additives, Fig. 11 presents the average skewness factor and flatness factor of the streamwise velocity fluctuation in the LES simulation. The skewness factor can describe the deviation between turbulent flow field and the Gaussian flow field where the skewness factor is 0. Fig. 11a shows that both Newtonian turbulent flow and non-Newtonian turbulent flow deviate from the Gaussian flow field, but larger deviations and higher asymmetry are found in non-Newtonian turbulent flow. In addition, with the increase of Weissenberg number, the skewness factor will increase too. Generally, the flatness factor can represent the overall intermittency of turbulent flow. From Fig. 11b it is easy to see that the flatness factor of Newtonian turbulent flow is larger than that of turbulent drag-reducing flow with surfactant additives, indicating that the probability density function of streamwise velocity in turbulent drag-reducing flow is flatter than that of Newtonian turbulent flow, the reason can be attributed to that the intermittency is suppressed and weakened by surfactant additives. From the analysis of skewness factor and flatness factor, it can be concluded that the overall intermittency of turbulent channel flow is suppressed and the turbulent fluctuation and burst events are obviously weakened with the adding of surfactant drag reducer.
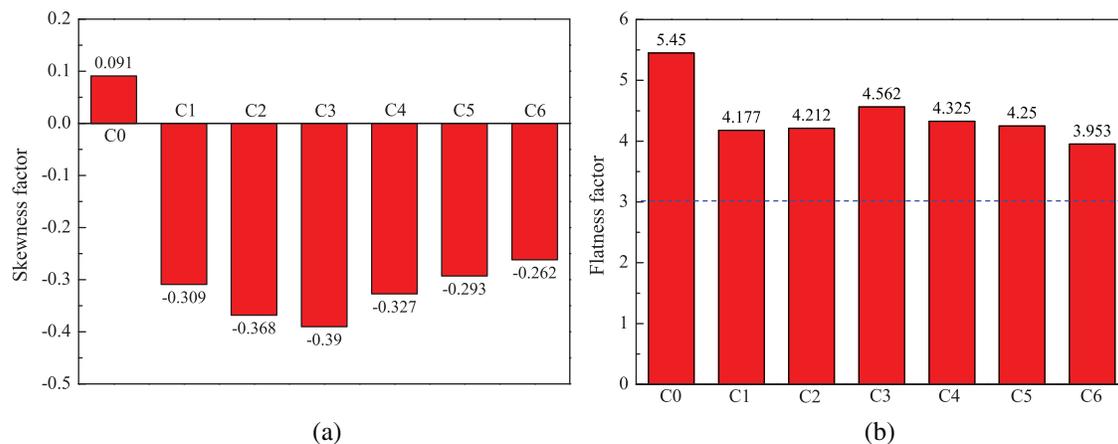

Figure 11: Average skewness factor and flatness factor. (a) Average skewness factor. (b) Average flatness factor

5 Conclusions

In this study, we implement the LES investigation of turbulent drag-reducing channel flow with surfactant additives using a hybrid subgrid scale model and a double-parallel FENE-P constitutive model. In the hybrid subgrid scale model, ICSM is applied to filter the momentum

equation and TADM is used to filter the double-parallel FENE-P model. The LES governing equations, numerical methods and algorithm are introduced in detail. The LES is first validated through commonly-used PIV experiments, in which the PIV measured results validate that the LES approach can offer a good prediction accuracy. Then seven numerical cases at high Reynolds number (the fraction Reynolds number is up to 600) and different solution concentrations (the Weissenberg number is 10~40 and β is 0.1~0.2) are simulated by the verified LES. Simulation results are displayed and drag-reducing mechanism is analyzed in detail from the perspectives of DR rate, streamwise mean velocity, RMS of deformation rate fluctuations, shear stress, transport and dissipation of turbulent kinetic energy, coherent structures, etc. It is noted that there exists distinctions in flow characteristics and drag-reducing mechanism between turbulent drag-reducing flows at high Reynolds number and low Reynolds number.

In this work, we have presented the application of a hybrid SGS model and N-parallel FENE-P model within LES to study the turbulent drag-reducing channel flow. As our next step, we aim to study the application of presented method for more complicated simulation conditions, such as different concentrations and different branches of parallel FENE-P model. Other possible research directions include extensions to the multiphase turbulent drag-reducing flow and turbulent flow with supercritical fluid.

Conflicts of Interest: The authors declare that they have no conflicts of interest to report regarding the present study.

References

1. Pope, S. B. (2001). *Turbulent flows*. Cambridge, United Kingdom: Cambridge University Press.
2. Mathieu, J., Scott, J. (2000). *An introduction to turbulent flow*. Cambridge, United Kingdom: Cambridge University Press.
3. Savins, J. G. (1964). Drag reduction characteristics of solutions of macromolecules in turbulent pipe flow. *Society of Petroleum Engineers Journal, 4(03),* 203–214. DOI 10.2118/867-PA.
4. Zakin, J. L., Lu, B., Bewersdorff, H. W. (1998). Surfactant drag reduction. *Reviews in Chemical Engineering, 14(4–5),* 253–320. DOI 10.1515/REVCE.1998.14.4-5.253.
5. Ptasinski, P., Boersma, B., Nieuwstadt, F., Hulsen, M., Van den Brule, B. et al. (2003). Turbulent channel flow near maximum drag reduction: simulations, experiments and mechanisms. *Journal of Fluid Mechanics, 490,* 251–291. DOI 10.1017/S0022112003005305.
6. Al-Sarkhi, A. (2010). Drag reduction with polymers in gas–liquid/liquid–liquid flows in pipes: a literature review. *Journal of Natural Gas Science and Engineering, 2(1),* 41–48. DOI 10.1016/j.jngse.2010.01.001.
7. White, C. M., Mungal, M. G. (2008). Mechanics and prediction of turbulent drag reduction with polymer additives. *Annual Review of Fluid Mechanics, 40(1),* 235–256. DOI 10.1146/annurev.fluid.40.111406.102156.
8. Wang, Y., Yu, B., Zakin, J. L., Shi, H. (2011). Review on drag reduction and its heat transfer by additives. *Advances in Mechanical Engineering, 2011,* 478749. DOI 10.1155/2011/478749.

9. Moin, P., Mahesh, K. (1998). Direct numerical simulation: a tool in turbulence research. *Annual Review of Fluid Mechanics, 30(1),* 539–578. DOI 10.1146/annurev.fluid.30.1.539.

10. Smagorinsky, J. (1963). General circulation experiments with the primitive equations: I. The basic experiment. *Monthly Weather Review, 91(3),* 99–164.

11. Iaccarino, G., Shaqfeh, E. S., Dubief, Y. (2010). Reynolds-averaged modeling of polymer drag reduction in turbulent flows. *Journal of Non-Newtonian Fluid Mechanics, 165(7–8),* 376–384. DOI 10.1016/j.jnnfm.2010.01.013.

12. Constantinescu, G. S., Squires, K. D. (2003). Les and des investigations of turbulent flow over a sphere at Re = 10,000. *Flow, Turbulence and Combustion, 70(1–4),* 267–298. DOI 10.1023/B:APPL.0000004937.34078.71.

13. Sagaut, P. (2006). *Large eddy simulation for incompressible flows: an introduction.* New York, United States: Springer Science & Business Media.

14. Germano, M., Piomelli, U., Moin, P., Cabot, W. H. (1991). A dynamic subgrid-scale eddy viscosity model. *Physics of Fluids A: Fluid Dynamics, 3(7),* 1760–1765. DOI 10.1063/1.857955.

15. Lilly, D. K. (1992). A proposed modification of the germano subgrid-scale closure method. *Physics of Fluids A: Fluid Dynamics, 4(3),* 633–635. DOI 10.1063/1.858280.

16. Liu, S., Meneveau, C., Katz, J. (1994). On the properties of similarity subgrid-scale models as deduced from measurements in a turbulent jet. *Journal of Fluid Mechanics, 275,* 83–119. DOI 10.1017/S0022112094002296.

17. Kobayashi, H. (2005). The subgrid-scale models based on coherent structures for rotating homogeneous turbulence and turbulent channel flow. *Physics of Fluids, 17(4),* 045104. DOI 10.1063/1.1874212.

18. Thais, L., Tejada-Martinez, A., Gatski, T., Mompean, G. (2010). Temporal large eddy simulations of turbulent viscoelastic drag reduction flows. *Physics of Fluids, 22(1),* 013103. DOI 10.1063/1.3294574.

19. Pruett, C. D. (2000). Eulerian time-domain filtering for spatial large-eddy simulation. *AIAA Journal, 38(9),* 1634–1642. DOI 10.2514/2.1146.

20. Pruett, C., Gatski, T., Grosch, C. E., Thacker, W. (2003). The temporally filtered navier–stokes equations: properties of the residual stress. *Physics of Fluids, 15(8),* 2127–2140. DOI 10.1063/1.1582858.

21. Pruett, C., Thomas, B., Grosch, C., Gatski, T. (2006). A temporal approximate deconvolution model for large-eddy simulation. *Physics of Fluids, 18(2),* 028104. DOI 10.1063/1.2173288.

22. Tejada-Martinez, A. E., Grosch, C. E., Gatski, T. B. (2007). Temporal large-eddy simulation of unstratified and stably stratified turbulent channel flows. *International Journal of Heat and Fluid Flow, 28(6),* 1244–1261. DOI 10.1016/j.ijheatfluidflow.2007.06.002.

23. Wang, L., Cai, W. H., Li, F. C. (2014). Large-eddy simulations of a forced homogeneous isotropic turbulence with polymer additives. *Chinese Physics B, 23(3),* 034701. DOI 10.1088/1674-1056/23/3/034701.

24. Li, F., Wang, L., Cai, W. (2015). A new mixed subgrid-scale model for large eddy simulation of turbulent drag-reducing flows of viscoelastic fluids. *Chinese Physics B, 24(7),* 074701. DOI 10.1088/1674-1056/24/7/074701.

25. Li, J., Yu, B., Wang, L., Li, F., Hou, L. (2017). A mixed subgrid-scale model based on icsm and tadm for les of surfactant-induced drag-reduction in turbulent channel flow. *Applied Thermal Engineering, 115,* 1322–1329. DOI 10.1016/j.applthermaleng.2016.11.112.

26. Ruettgers, M., Park, J., You, D. (2019). Large-eddy simulation of turbulent flow over the drivaer fastback vehicle model. *Journal of Wind Engineering and Industrial Aerodynamics, 186,* 123–138. DOI 10.1016/j.jweia.2019.01.003.

27. Lian, Y., Dallmann, J., Sonin, B., Roche, K., Liu, W. K. et al. (2019). Large eddy simulation of turbulent flow over and through a rough permeable bed. *Computers & Fluids, 180,* 128–138. DOI 10.1016/j.compfluid.2018.12.015.

28. Chen, Y., Djidjeli, K., Xie, Z. T. (2020). Large eddy simulation of flow past stationary and oscillating square cylinders. *Journal of Fluids and Structures, 97,* 103107. DOI 10.1016/j.jfluidstructs.2020.103107.

29. Evrim, C., Laurien, E. (2020). Large-eddy simulation of turbulent thermal flow mixing in a vertical T-junction configuration. *International Journal of Thermal Sciences, 150,* 106231. DOI 10.1016/j.ijthermalsci.2019.106231.

30. Li, J., Yu, B., Sun, S., Sun, D., Kawaguchi, Y. (2018). An N-parallel FENE-P constitutive model and its application in large-eddy simulation of viscoelastic turbulent drag-reducing flow. *Journal of Computational Science, 29,* 70–80. DOI 10.1016/j.jocs.2018.09.016.

31. Li, J., Yu, B., Wang, Y., Tang, Y., Wang, H. (2015). Study on computational efficiency of composite schemes for convection-diffusion equations using single-grid and multigrid methods. *Journal of Thermal Science and Technology, 10(1),* JTST0009. DOI 10.1299/jtst.2015jtst0009.

32. Li, J., Yu, B., Zhao, Y., Wang, Y., Li, W. (2014). Flux conservation principle on construction of residual restriction operators for multigrid method. *International Communications in Heat and Mass Transfer, 54,* 60–66. DOI 10.1016/j.icheatmasstransfer.2014.03.013.

33. Fu, Z., Otsuki, T., Motozawa, M., Kurosawa, T., Yu, B. et al. (2014). Experimental investigation of polymer diffusion in the drag-reduced turbulent channel flow of inhomogeneous solution. *International Journal of Heat and Mass Transfer, 77,* 860–873. DOI 10.1016/j.ijheatmasstransfer.2014.06.016.

34. Li, F. C., Yu, B., Wei, J. J., Kawaguchi, Y. (2012). *Turbulent drag reduction by surfactant additives.* New York, United States: John Wiley & Sons.

35. Hunt, J. C., Wray, A. A., Moin, P. (1988). Eddies, streams, and convergence zones in turbulent flows. *Studying Turbulence Using Numerical Simulation Databases, 2, 1,* 193–208.